Research Article

Nano Research
2022, 15(7): 5884–5894

ISSN 1998-0124 CN 11-5974/O4
https://doi.org/10.1007/s12274-022-4231-8

Surface modification of metal-organic frameworks under sublimated iron-atmosphere by controlled carbonization for boosted oxygen evolution reaction

Katam Srinivas[1,§], Xin Chen[1,§], Dawei Liu[1], Fei Ma[1], Xiaojuan Zhang[1], Wanli Zhang[1], Hua Lin[2] (✉), and Yuanfu Chen[1,3] (✉)

[1] *School of Electronic Science and Engineering, and State Key Laboratory of Electronic Thin Films and Integrated Devices, University of Electronic Science and Technology of China, Chengdu 610054, China*
[2] *School of Materials and Energy, Southwest University, Chongqing 400715, China*
[3] *College of Science, and Institute of Oxygen Supply, Tibet University, Lhasa 850000, China*
[§] *Katam Srinivas and Xin Chen contributed equally to this work.*

Received: 15 December 2021 / **Revised:** 8 February 2022 / **Accepted:** 13 February 2022

ABSTRACT

Development of cost-effective, efficient, and durable electrocatalysts for oxygen evolution reaction (OER) with fast kinetic reaction is highly significant, considering the elevated thermodynamic energy barrier involved in water electrolysis. To overcome such challenges, an innovative vapor phased iron-doping strategy is employed on carbon nanotubes (CNT)-interlinked metal-organic framework (MOF) nanosheets (Ni-MOF@CNT) to obtain mixed metal oxide and metal heteronanoparticles superficially implanted partially (*semi*)-decomposed MOF nanosheets (Ni-M@C-400). These *semi*-MOF nanosheets attain the structural privileges related to MOF-nanostructure, mixed metal nanoparticles synergism, interconnected-CNT assisted high conductivity, and mechanical strength. As a result, Ni-M@C-400 exhibits exceptional OER activity with overpotential as low as 229 mV to reach the benchmark current density of 10 mA/cm^2 (η_{10}) and exhibits greatly reduced thermodynamic barrier (Tafel slopes of 40.51 mV/dec) along with significant durability for ~ 60 h. More importantly, this sublimated iron-doped *semi*-MOF (Ni-M@C-400) displays significantly better OER performance over the corresponding annealed bimetallic MOF (NiFe-M@C-400: 270 mV at η_{10}). Moreover, the successful incorporation of vapor phased iron into variety of MOFs (Cr, Mn, Co, Ni, and Cu) approved its uniqueness and the universality. This work provides an innovative vapor phased heteroatom-doping strategy to develop cost-effective and efficient electrocatalysts for water electrolysis.

KEYWORDS

metal-organic frameworks (MOFs), *semi*-MOFs, controlled carbonization, heteronanoparticles, oxygen evolution reaction

1 Introduction

Systematic design and utilization of sustainable energy production technologies have gained enormous attention in recent years considering the continuously rising global energy demands and enormously diminishing natural energy resources [1–4]. As a matter of fact, electrocatalytic water splitting is greatly appreciated for its sustainable hydrogen production with extremely easy set-up and handling ability [5–7]. Particularly, water electrolysis involves the decomposition of water into hydrogen and oxygen gases by means of hydrogen evolution reaction (HER) and oxygen evolution reaction (OER), respectively. Despite that, the unfavorable reaction kinetics involved in OER process endorsed to be the bottle-neck in deciding the overall efficiency of water splitting [8–11]. Thankfully, the precious metal-based oxides including IrO_2 and RuO_2 demonstrated noteworthy performance towards OER by diminishing the thermodynamic barrier. However, their limited reserves, unaffordable cost, and poor long-range maintainability in harsh alkaline environment make them inappropriate to be considered for large-scale usage. As a result, it is highly indispensable to design non-precious alternative electrocatalysts with significantly competitive performances and durability in affordable price.

Considering the significance of water electrolysis, wide variety of cost-effective transition metal-based electrocatalysts have been developed and noticed substantially improved performances with excellent long-term operation abilities [12–18]. Particularly, due to the diversified topologies, large surface areas, adjustable porous nature, and tenability to introduce multi-metals, a vast number of metal-organic frameworks (MOFs) and their composites used as electrocatalysts toward water electrolysis [19–22]. Interestingly, the OER activity of a pristine MOF is enormously enhanced by introducing the second or third metal into the MOF construction. Additional metal incorporation basically adjusts the intrinsic electrical conductivity of a material and modulates its surface to expose vast number of active sites for improved performance [23]. In particular, Ni/Fe-, Co/Fe-, and Ni/Co- combinations are widely studied in water electrolysis, owing to their vast terrestrial abundance, facile and low-cost fabrication methods, and enhanced

Address correspondence to Hua Lin, lh2004@swu.edu.cn; Yuanfu Chen, yfchen@uestc.edu.cn

structural and mechanical stability [24]. Recent literature studies approved the crucial surface electronic states modification in Ni-based electrocatalysts (Ni^{2+} to $Ni^{3+/4+}$) by means of Fe-incorporation and that phenomenon significantly boosts the OER performance and also helps maintaining the overall composition of material during long-time operations [13]. In addition, the importance of Fe and its effective synergism with Ni has also been established recently. Specifically, a small traces of Fe in $Ni(OH)_2$ proved to enhance the OER activity [25–27] and more importantly $NiFeO_xH_y$ is established as one of the best OER electrocatalysts reported to date [28].

But to our surprise, most of the established methods dealt with the incorporation of multi-metal sources during the material preparation stage, but integration of secondary metal by any other methods is hardly been established [12–14]. However, introducing the secondary metal sites precisely on the materials surface by systematic surface engineering strategy for a particular functionality is scarcely been reported [15, 19, 29, 30], and in most cases, the proposed methods have not been subjected to variety of precursor systems [20]. Besides, considering the deprived electrical conductivity, seldom mechanical, thermal, and chemical stability during long-time operations, MOFs are mainly used as sacrificial templates to obtain MOF-derived materials, and assimilated their water splitting abilities [22, 31]. Moreover, the high temperature annealing often resulted in reduced specific surface area with demolished porous network and the bulk material formed by MOF-decomposition seize the active species, which make MOF-derived materials incompatible for water electrolysis [32]. Fascinatingly, controlled annealing strategy of a MOF to accomplish active species within its architecture with combined advantages of MOFs and MOF-derived materials only by regulating the annealing temperature has gained much research significance in recent years [32–36]. Despite delivering the exceptional water splitting performances, this strategy is still in its embryonic stage.

Therefore, considering the above stated issues, herein, we have opted for a systematic surface engineering of a MOF by controlled carbonization under sublimated iron-atmosphere. Notably, the regulated annealing yields *semi*-MOF composites with embedded nanoparticles, meanwhile vaporized Fe can interact with the newly produced nanoparticles on the materials surface in order to develop Fe-doped composition. Among the annealed samples, the *semi*-MOF fabricated at 400 °C (Ni-M@C-400) with partially decomposed MOF nanosheet-architecture along with newly implanted active nanoparticles ($Ni_{0.4}Fe_{2.6}O_4$ and Ni) acquire the advantages associated to MOF-nanostructure, active nanoparticles synergism and the carbon nanotube (CNT)-related enhanced electrical and mechanical strength. As a consequence, Ni-M@C-400 displays exceptional water oxidation performance (overpotential at 10 mA/cm^2 = 229 mV; Tafel slope = 40.51 mV/dec) surpassing the RuO_2 performance and the other transition metal-based state-of-the-art electrocatalysts (Table S1 in the Electronic Supplementary Material (ESM)). Besides, the successful incorporation of Fe- into the CNT-integrated Cr, Mn, Co, and Cu MOFs approves its universality. Surprisingly, the bimetallic Ni/Fe- and Co/Fe- MOFs witnessed the maximum decomposition of MOF-skeleton under the same set of annealing conditions and thereby displayed relatively low OER activity. Therefore, it is believed that the innovative Fe-doping approach presented herein can be applied to various material systems to design template directed electrocatalysts in view of developing the cost-effective and efficient electrocatalysts for vast variety of energy conversion processes.

2 Experimental section

2.1 Material fabrication approach

2.1.1 Fabrication of Fe-doped Ni-MOF-derivatives

Carbon nanotubes-interlinked Ni-based porous MOF nanosheets (Ni-MOF@CNT) were fabricated following our earlier report [37, 38], briefly from a reaction between $Ni(NO_3)_2{\cdot}6H_2O$ and 1,4-benzenedicarboxylic acid (1,4-BDC) in a mixed N,N-dimethylformamide (DMF), ethanol (C_2H_5OH), and water solution. Now, 270 mg of $FeCl_3{\cdot}6H_2O$ (1 mmol) and 250 mg of pristine Ni-MOF@CNT were taken in a quartz boat for controlled carbonization treatment and made sure that the Fe-source occupies the upstream side of N_2 gas flow. Subsequently, the furnace temperature was raised to 400 °C with a rampage rate of 5 °C/min and maintained for 3 h. The as-obtained sample after annealing process was denoted as Ni-M@C-400. Afterwards, in view of elucidating the annealing temperature effect, the carbonization was carried out at slightly higher temperatures, such as 500 °C (Ni-M@C-500) and 600 °C (Ni-M@C-600) keeping the reaction time and weights of $FeCl_3{\cdot}6H_2O$ and Ni-MOF@CNT constant.

Afterwards, in view of realizing the influence of sublimated Fe-doping technique, bimetallic NiFe-MOF@CNT and CoFe-MOF@CNT have been prepared in the same manner using 1:1:2 mole ratio of Ni^{2+}:Fe^{3+}:1,4-BDC and Co^{2+}:Fe^{3+}:1,4-BDC reagents, respectively. Subsequently, both the MOFs have been subjected to 400 °C annealing for 3 h in order to comprehend the morphological and performance related information and the obtained annealed samples have been denoted as NiFe-M@C-400 and CoFe-M@C-400, respectively.

2.1.2 Fabrication of Fe-doped Cr, Mn, Co, and Cu based semi-MOFs

Analogous Cr-MOF@CNT, Mn-MOF@CNT, Co-MOF@CNT, and Cu-MOF@CNT samples have been prepared in the same manner as described for Ni-MOF@CNT, except that the metal source was changed to $Cr(NO_3)_3{\cdot}9H_2O$, $Mn(NO_3)_2{\cdot}4H_2O$, $Co(NO_3)_2{\cdot}6H_2O$, and $Cu(NO_3)_2{\cdot}3H_2O$, respectively. Subsequently, 270 mg of $FeCl_3{\cdot}6H_2O$ (1 mmol) and 250 mg of pristine MOF@CNT were placed in a quartz boat and subjected to controlled decomposition under flowing N_2 gas. The as-obtained annealed derivatives have been named as Cr-M@C-400, Mn-M@C-400, Co-M@C-400, and Cu-M@C-400.

2.2 Materials characterization

2.2.1 Materials-structure and morphology evaluation

Crystalline patterns and the phase purity of as-prepared MOFs and MOF-derived materials have been elucidated by X-ray diffraction (XRD) study (Rigaku D/MAX-rA diffractometer with Cu Kα radiation source). Chemical composition and their oxidation states in Ni-M@C-400 and Co-M@C-400 have been realized by X-ray photoelectron spectroscopy (XPS) analysis (Kratos XSAM800 with monochromatic Al-Kα source). Raman analysis of Ni-MOF, Co-MOF, and their derivatives have been realized by confocal Raman microscope (Renishaw Corporation, excitation wavelength was 532 nm). The thermal decomposition pathway of pristine MOF (Ni-MOF@CNT) was investigated by thermogravimetric analysis (TGA, SDT Q600). Morphologies of various MOFs and corresponding derivatives were evidenced by field-emission scanning electron microscopy (FE-SEM, FEI Quanta 650 SEM), while the Ni-M@C-400 (*semi*-MOF) nanostructure and the corresponding lattice fringes have been

manifested from high-resolution transmission electron microscopy (HR-TEM, Titan G260-300). Similarly, the available surface area and the porous nature of Ni-M@C-400 were estimated by N_2 adsorption–desorption isotherms (Brunauer–Emmett–Teller theory, Quantachrome, Nova 2000e).

2.2.2 *Water oxidation performance evaluation*

Water electrolysis performance of all the new samples prepared has been investigated in 1 M potassium hydroxide (KOH) solution using a standard three-electrode set-up assembled by catalysts modified glassy carbon electrode (GCE, working electrode), counter electrode (graphite rod), and a reference electrode (Hg/HgO electrode) utilizing the CHI 660D electrochemical work station. First of all, 4 mg of as-prepared sample was dispersed in 1 mL of distilled water and ethanol mixture (3:1 of v/v) by ultrasonication for 5 min, followed by addition of 50 μL of Nafion ink and then ultrasonication was continued for additional 30 min. As-obtained catalysts ink was drop-casted on polished GC electrodes (diameter = 0.003 m and catalyst loading = 0.28 mg/cm^2) and dried in an electric oven for 10 min prior to water electrolysis test. These catalysts loaded GC electrodes have been subjected to cyclic voltammetry tests (20 CV cycles) in order to activate the material before being realized the linear sweep voltammetry (LSV) curves. The LSV tests have been carried out at 5 mV/s scan rate in view to evaluating the overpotentials at different current densities (j) and afterwards, the obtained LSV plots have been used to assess the corresponding Tafel slopes in view of investigating the reaction kinetics. Particularly, the potential values obtained using Hg/HgO reference electrode were calibrated versus reversible hydrogen electrode (RHE) using the equation of $E_{RHE} = E_{Hg/HgO} + 0.923$ V and the overpotentials presented in this study were estimated from the LSV plots using the equation of $E_{RHE} - 1.23$ V. Besides, the accessible electrochemical active surface area (ECSA) of as-prepared electrocatalysts was evaluated by conducting cyclic voltammograms within a non-Faradic current region. While the charge-transfer capabilities and the electrode/electrolyte interface resistance were investigated by electrochemical impedance spectroscopy (EIS, frequency range = 100 kHz to 0.1 Hz). Moreover, the CV cycling stability was assessed by 2,000 continuous CV cycles on GC electrode, while the long-time i–t (chronoamperometry test) was performed on Ni foam current collector (1 cm × 2 cm, catalyst loading was 2 mg/cm^2).

3 Results and discussion

3.1 Systematic fabrication and evaluation of Ni/Fe-based *semi*-MOFs

Electrochemically active nanoparticles implanted *semi*-MOFs have been fabricated by a unique vapor phased iron-doping strategy into a series of earth-abundant transition metal-based pristine MOFs. At first, Ni-MOF and its CNT-composite have been fabricated following our earlier report and the XRD patterns approved the MIL-type of MOF coordination (Fig. S1(a) in the ESM) [37]. Initially, the Ni-MOF@CNT was subjected to TGA analysis in order to figure out its thermal behavior. According to Fig. 1(a), a gradual loss in weight was noticed until 300 °C (~ 5% weight loss) that corresponds to the removal of adsorbed water and the solvent molecules, while the actual MOF-decomposition begins at 400 °C, and the maximum organic unit's decomposition can be realized at 450 °C. Therefore, based on the TGA data, the Ni-MOF@CNT was first subjected to partial decomposition at 400 °C and as anticipated Ni nanoparticles implanted *semi*-MOF (Ni@*semi*-MOF) was obtained (Fig. S1(b) in the ESM). In general, MOFs upon high temperature annealing produce metal nanoparticles embedded porous carbon, as this Ni-MOF@CNT was carbonized at a controlled annealing temperature, the as-obtained material demonstrated Ni nanoparticles within partially decomposed MOF. Recent pioneering research efforts approved that the sublimated heteroatoms such as S, Se, and P can be introduced into the MOF during carbonization leading to the successful isolation of metal chalcogenides and/or phosphides [5, 39, 40]. While the sublimated heterometal-doping during carbonization is scarcely been reported. To be specific, Sun et al. established the effective incorporation of sublimated Fe into the zeolitic imidazole framework-8 (ZIF-8) derived porous carbon [41], and Liang et al. demonstrated the successful utilization of sublimated Fe in fabricating the heterogeneous $CoFe_2O_4/CoO_x$ electrocatalysts [42].

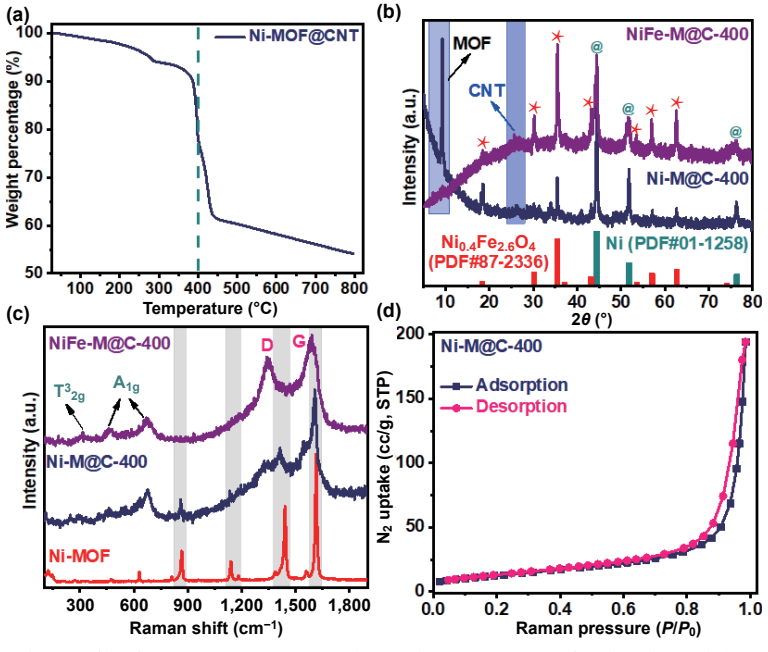

Figure 1 (a) Thermogravimetric analysis profile of pristine Ni-MOF@CNT, (b) powder XRD patterns of Ni-based annealed MOFs, (c) Raman spectral data of Ni-based annealed MOFs, and (d) specific surface area profile of Ni-M@C-400.

On the basis of above experimental results and the discussion, $FeCl_3·6H_2O$ has been considered as an appropriate Fe-source owing to its low sublimation point (280–285 °C), and placed this iron-source at the upstream position of N_2 gas flow in addition to the Ni-MOF@CNT and subjected to controlled annealing temperature at 400 °C [32, 43]. For the as-obtained Ni-M@C-400 material, XRD patterns disclosed the presence of remnant MOF peak at 9.2° and the co-existence of $Ni_{0.4}Fe_{2.6}O_4$ (JCPDS No. 87-2336) and Ni (JCPDS No. 01-1258) heteronanoparticles within the CNT-network (Scheme 1 and Fig. 1(b)). While, the XRD patterns of MOF annealed at higher temperature (Ni-M@C-500) under Fe-vapor approved the complete MOF-decomposition and displayed $Ni_{0.4}Fe_{2.6}O_4$ and Ni heteronanoparticles within the CNT-network (Fig. S2(a) in the ESM). Surprisingly, further increase in annealing temperature to 600 °C (Ni-M@C-600) produced the unique NiFe alloy composition within CNT-network (Fig. S2(b) in the ESM). Aforementioned TGA and XRD investigations indicate that the 400 °C annealing under Fe-vapor only can yield the heteronanoparticles embedded *semi*-MOF. Besides that, the bimetallic NiFe-MOF@CNT carbonized under the same set of conditions (400 °C for 3 h; NiFe-M@C-400; without additional Fe-source) demonstrated the significant decrease in MOF peak ((100) crystal plane of MOF at 9.2°), which approves the maximum decomposition of MOF-skeleton, despite approving the presence of $Ni_{0.4}Fe_{2.6}O_4$ (JCPDS No. 87-2336), and Ni (JCPDS No. 01-1258) combination in its XRD analysis (Fig. 1(b)). This further approves the significance of sublimated Fe-doping strategy in fabricating the active nanoparticles implanted *semi*-MOFs.

Besides, in order to realize the universality of vapor phased Fe-doping strategy, Co-MOF@CNT has been subjected to controlled annealing under vaporized Fe-source (Co-M@C-400) and to our surprise, it yields only $CoFe_2O_4$ nanoparticles within *semi*-MOF composite (Fig. S2(c) in the ESM). Evidently, the bimetallic CoFe-MOF@CNT upon controlled annealing (CoFe-M@C-400) yielded the cobalt ferrite nanoparticles within extensively decomposed MOF. Besides, high temperature annealing (Co-M@C-500) produced the combination of $CoFe_2O_4$ and Co heteronanoparticles within CNT-matrix similar to Ni-M@C-500 (Fig. S2(d) in the ESM) [43]. Subsequently, this new strategy has been extended to Cr-MOF@CNT, Mn-MOF@CNT, and Cu-MOF@CNT. Wherein, Cr- and Mn- MOFs produced the corresponding ferrite nanoparticles (MFe_2O_4: M = Cr or Mn) within partially decomposed MOF [44], while the Cu-MOF@CNT delivered the combination of $Cu_{0.86}Fe_{2.14}O_4$ and Cu heteronanoparticles within the remnant MOF (Fig. S3 in the ESM) [45]. Moreover, due to the high crystalline nature of metal-constituents, the carbon nanotubes diffraction peaks are rather invisible in aforementioned samples, but are unambiguously determined by the characteristic D and G bands of CNT in their Raman spectral analysis (Fig. 1(c), and Figs. S4(a) and S4(b) in the ESM) [46–48]. Figure 1(c) presents the data of Raman spectra of pristine Ni-MOF and its corresponding annealed derivative (Ni-M@C-400) in comparison with extensively decomposed bimetallic MOF (NiFe-M@C-400). Precisely, the characteristic Raman bands of Ni-MOF (related to 1,4-BDC) unambiguously detected in Ni-M@C-400 at 1,615 and 1,440 cm^{-1} ($-COO_{stretching}$), 1,140 cm^{-1} ($C-O_{bending}$), and 865 and 630 cm^{-1} ($C-H_{stretching}$) [14, 49], confirming the *semi*-MOF composition even after annealing treatment, while the same are almost disappeared in NiFe-M@C-400 as it undergoes maximum decomposition.

In addition, the formation of $Ni_{0.4}Fe_{2.6}O_4$ has been evidenced by the existence of T^3_{2g} (~ 315 cm^{-1}) and A_{1g} (~ 462 and 675 cm^{-1}) peaks in both Ni-M@C-400 and NiFe-M@C-400 samples (Fig. 1(c)) [50]. Besides, Ni-M@C-500 also displayed the characteristic Raman bands of nickel ferrite at ~ 203 cm^{-1} (T^1_{2g}), 322 cm^{-1} (T^3_{2g}), 567 cm^{-1} (T^2_{2g}), and 674 cm^{-1} (A_{1g}), as it also possessed the $Ni_{0.4}Fe_{2.6}O_4$/Ni heteronanoparticles composition. Evidently, pristine MOF related bands are disappeared in both Ni-M@C-500 and Ni-M@C-600 as they underwent complete decomposition (Fig. S4(a) in the ESM). In the same way, Co-M@C-400 and the bimetallic CoFe-M@C-400 displayed the characteristic Raman bands correspond to $CoFe_2O_4$ at 312 cm^{-1} (E_g), 460 cm^{-1} (T_{2g}), and 672 cm^{-1} (A_{1g}) as both of them yielded the same composition but the former evidenced the additional peaks at 860, 1,132, 1,423, and 1,628 cm^{-1} correspond to Co-MOF in approving its partial decomposition (Fig. S4(b) in the ESM) [51]. All these experimental results revealed the fact that 400 °C annealing is favorable for *semi*-MOFs fabrication, and the aforementioned results collectively summarized that the newly established Fe-doping strategy can be successfully implemented to variety of MOF-systems in order to fabricate the surface modified electrocatalysts.

Additionally, the N_2 adsorption–desorption isotherm of Ni-M@C-400 displayed considerably high specific surface area of 56.95 m^2/g owing to its partially decomposed MOF-skeleton. Notably, very high pore diameter of 20.95 nm has been detected for Ni-M@C-400 (Fig. S4(c) in the ESM), which can allow the electrolyte penetration through the material for enhanced water electrolysis. Moreover, small hysteresis curve noticed within 0.4 to 0.6 relative pressures (P/P_0) range signifying the presence of beneficial *micro*- and *meso*-pores, and the high N_2 uptake between 0.8 to 1.0 P/P_0 range suggests the possible *meso*- and *macro*-pores in Ni-M@C-400 (Fig. 1(d)) [52].

Scanning electron microscopy (SEM) approves the ultrathin porous two-dimensional (2D) nanosheet morphology of Ni-MOF and upon CNT-integration (Ni-MOF@CNT), the porous sheet-like morphology transformed to CNT-interconnected individual porous nanosheets (Figs. 2(a) and 2(b), and Figs. S5(a)–S5(c) in the ESM) and almost the same morphology noticed for NiFe-MOF@CNT with slightly exposed CNT-network (Fig. S5(d) in the ESM). Besides, SEM analysis of Ni-M@C-400 clearly demonstrated the partially crumbled MOF-nanosheets

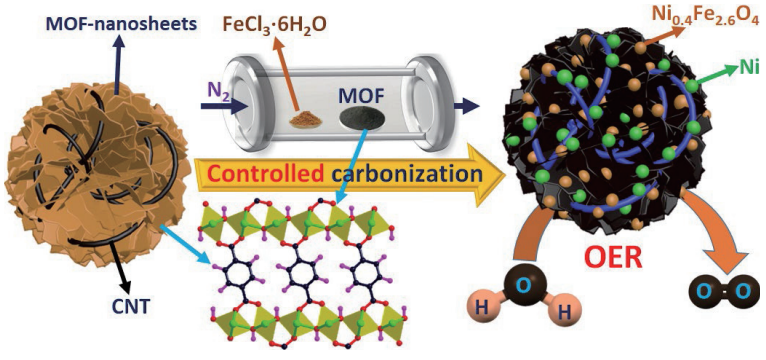

Scheme 1 Schematic illustration of heteronanoparticles implanted partially decomposed MOFs (*semi*-MOFs) by means of vapor phased Fe-doping strategy.

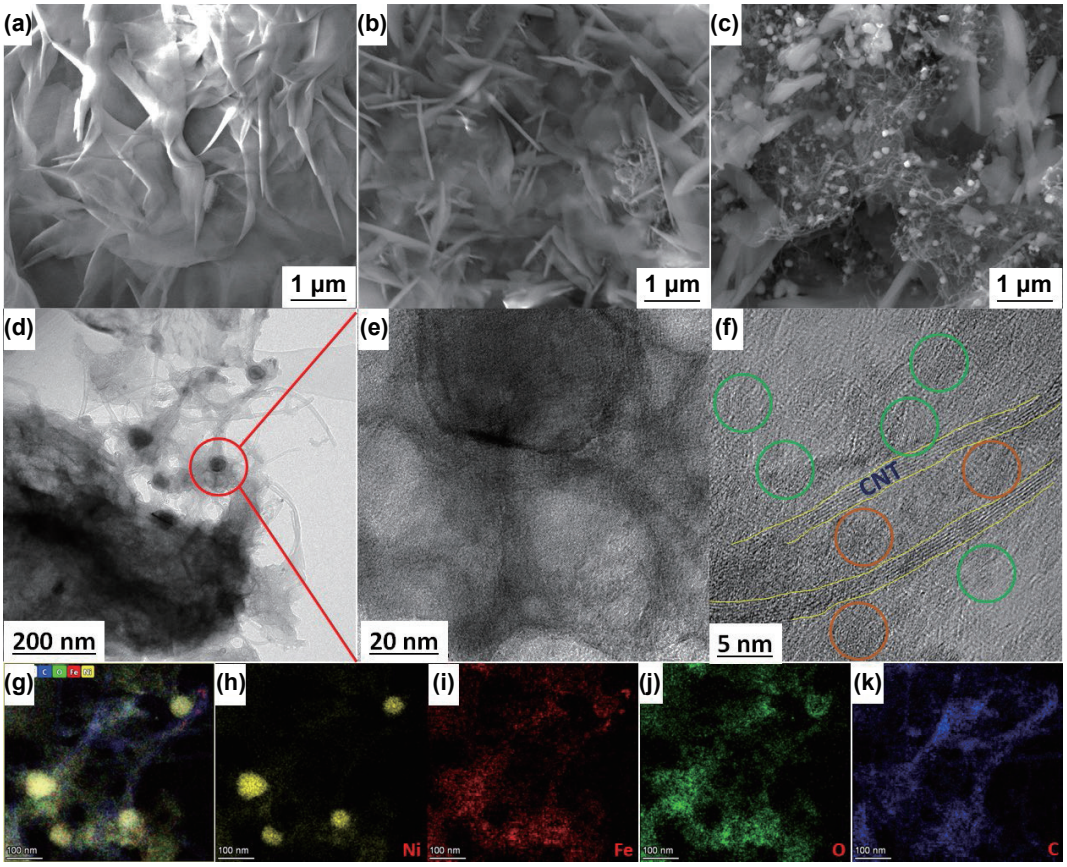

Figure 2 (a)–(c) SEM images of Ni-MOF, Ni-MOF@CNT, and Ni-M@C-400, respectively, (d)–(f) TEM and HR-TEM images of Ni-M@C-400 (green circles represent the lattice fringes of Ni and the brown circles correspond to the $Ni_{0.4}Fe_{2.6}O_4$ lattice fringes), and (g)–(k) HAADF-STEM and EDS-mapping images of Ni-M@C-400.

morphology with interlinked CNT-network fastened by active $Ni_{0.4}Fe_{2.6}O_4$/Ni heteronanoparticles (Fig. 2(c), and Figs. S6(a) and S6(b) in the ESM), similar morphology transformation was noticed for NiFe-M@C-400, wherein MOF-nanosheets have been mostly converted to nanoparticles and have interlinked by CNT-network and few broken MOF-nanosheets can be clearly visible in supporting the *semi*-MOF composition (Fig. S7 in the ESM). While, MOF-nanosheets complete decomposition into $Ni_{0.4}Fe_{2.6}O_4$/Ni heterostructure fastened by CNT-network has been clearly evidenced in Ni-M@C-500 (Figs. S6(c) and S6(d) in the ESM), and interestingly, large sized NiFe-alloy particles (more than 100 nm) connected by CNT-matrix was detected in the high temperature annealed sample under Fe-vapor (Ni-M@C-600) by complete decomposition of MOF-sheets (Figs. S6(e) and S6(f) in the ESM). Contrarily, porous sheets accumulated rectangular blocks in CNT-mesh morphology was detected for Co-MOF@CNT and was transformed to compressed nanoplates-like CNT-composite upon controlled carbonization under Fe-vapor (Co-M@C-400; Fig. S8 in the ESM). Additionally, the unique porous MOF-nanosheets interlinked by CNT-framework structure has been clearly detected in TEM analysis of Ni-M@C-400 (Fig. 2(d) and Fig. S9 in the ESM). Basically, pristine MOFs upon high temperature annealing under inert atmosphere produce corresponding metal nanoparticles embedded carbon matrix, and as we have systematically decomposed the Ni-MOF into its *semi*-MOF, Ni nanoparticles have been derived from the corresponding nanosheets [38]. As it was established earlier, the newly implanted nanoparticles can either be located on the surface of material [33, 35, 36] or distributed on the surface and/or inner part of the MOF-nanostructure [32]. In particular, the randomly distributed bright spots represent the nanosheets-derived Ni nanoparticles (Fig. 2(c) and Fig. S9 in the ESM).

Subsequently, the Ni-source presented on the surface (Ni nanoparticles and the Ni–O bonds of crumbled MOF) transformed to $Ni_{0.4}Fe_{2.6}O_4$ in the presence of sublimated Fe during carbonization. As a result, the surface mostly occupied by $Ni_{0.4}Fe_{2.6}O_4$ nanoparticles which are confirmed by the (311) crystal plane detected in HR-TEM images (brown circles in Fig. 2(f) with 0.252 nm interplanar spacing). While, the lattice fringes correspond to bright spots (Ni nanoparticles) are overshadowed due to the surface nickel ferrite formation, however, they can be unambiguously determined in various locations ((111) crystal plane with 0.204 nm interplanar distance; green circles in Fig. 2(f)). Precisely, the growth of Ni nanoparticles and the Fe-doping take place at the same time, hence the surface of Ni-M@C-400 mostly occupied by $Ni_{0.4}Fe_{2.6}O_4$ and the uniform distribution of Fe on materials surface can be realized from its high-angle annular dark-field scanning TEM (HAADF-STEM) and energy dispersive spectroscopy (EDS) data (Figs. 2(g)–2(k) and Fig. S10 in the ESM). In particular, the EDS-elemental mapping data approved that the bright spots in TEM images are the MOF-derived Ni nanoparticles (Fig. 2(h)) and also confirm the iron uniform distribution in the material (Fig. 2(i)). Similar such Fe-layered NiCo alloy within a *semi*-MOF was fabricated by Li et al. from a pristine NiCoFe-MOF by a controlled decomposition strategy. In which, the NiCo alloy formation (via Ni–O and Co–O bond breakage) takes place much faster than the Fe_3O_4 owing to the low Ni–O and Co–O bond energy, and hence the lately formed Fe_3O_4 (via Fe–O bond breakage) occupies the surface of NiCo alloy. Density functional theory (DFT) calculations also approved that this type of hetero composition enhances the OER performance by means of exchange stabilization phenomenon of active oxygen units [32].

Moreover, the existing elemental composition and their

corresponding oxidation states on the surface of Ni-M@C-400 have been elucidated by XPS measurement. As anticipated, this Fe-doped *semi*-MOF confirmed the co-existence of Ni, Fe, O, and C elements on its surface (Fig. 3(b)). Moreover, the Ni 2p XPS spectra displayed two main peaks at 856.42 eV (Ni $2p_{3/2}$) and 874.02 eV (Ni $2p_{1/2}$) correspond to Ni^{2+} oxidation state together with associated satellite peaks at 861.91 and 880.28 eV (Fig. 3(c)) [53]. The peak positions approved the negative shift in binding energies (~ 0.44 eV) for Ni $2p_{3/2}$ and Ni $2p_{1/2}$ compared to its pristine MOF, which confirms the modified electronic states of Ni after carbonization, as it develops nickel ferrite nanoparticles within its architecture [38, 54]. Although, the existence of Ni^0 in Ni-M@C-400 was unambiguously detected by XRD and EDS-mapping analysis, the corresponding peak appeared to be almost invisible (853.8 eV) in its surface analysis, confirming that most of the Ni^0 internally occupied in the material compared to the materials surface. This theory was well supported by the Ni:Fe metal ratio detected by XPS survey on Ni-M@C-400 surface (1:1.2) and the internal metal ratio detected by EDS elemental analysis (1:0.5) (Fig. 3(a)).

In addition, the Fe 2p XPS spectra displayed two main peaks with corresponding satellite peaks, in which the peaks positioned at 710.58 eV (Fe $2p_{3/2}$) and 723.63 eV (Fe $2p_{1/2}$) represent the presence of Fe^{2+} oxidation state of iron, and the other two peaks positioned at 712.61 eV (Fe $2p_{3/2}$) and 724.8 eV (Fe $2p_{1/2}$) correspond to the Fe^{3+} oxidation state of iron (Fig. 3(d)) [53]. In particular, the peak positions of Fe $2p_{3/2}$ and Fe $2p_{1/2}$ are considerably lowered (~ 0.42 to 1.17 eV) compared to the reported $NiFe_2O_4$-based materials [22, 53, 55], which means the Fe-metal center possesses high electron density in its 3d-orbitals and thereby converts into Fe–O(OH) state during water oxidation [13, 37]. The change in electron density and the shift in peak position for both Ni 2p and Fe 2p XPS spectra, approved the significant electronic interactions between two metals [53]. Moreover, the presence of Ni^0, Ni^{2+}, Fe^{2+}, and Fe^{3+} oxidation states of elements in Ni-M@C-400 approved the presence of $Ni/Ni_{0.4}Fe_{2.6}O_4$ combination.

Similarly, XPS spectral analysis of Co-M@C-400 approved the co-existence of Co, Fe, O, and C elements as expected. The core-level Co 2p spectra displayed two main peaks correspond to Co $2p_{3/2}$ and Co $2p_{1/2}$ with associated satellite peaks (787.24 and 803.87 eV). The main peaks further deconvoluted into two independent peaks correspond to Co^{3+} (781.58 and 797.52 eV) and Co^{2+} (783.31 and 799.43 eV) oxidation states of cobalt (Fig. 3(e)) [56]. While, the Fe 2p spectrum deconvoluted into two main peaks correspond to Fe $2p_{3/2}$ (710.73 and 713.49 eV) and Fe $2p_{1/2}$ (723.4 and 724.82 eV) with associated satellite peaks (787.24 and 803.87 eV; Fig. 3(f)). The peak positions and the oxidation states of Co (Co^{3+} and Co^{2+}) and Fe (Fe^{2+} and Fe^{3+}) elements in corresponding XPS spectral analysis are well matched with the XPS data reported for $CoFe_2O_4$-based materials, in supporting the existence of $CoFe_2O_4$ in Co-M@C-400 [56, 57]. Besides, the oxygen 1s XPS spectra of both the samples displayed two main peaks corresponding to metal–oxygen bonding peak (M–O; ~ 532.17 eV) attributed to the $Ni_{0.4}Fe_{2.6}O_4$ in Ni-M@C-400 and/or $CoFe_2O_4$ in Co-M@C-400 or M–O bond of *semi*-MOF along with the other metal–hydroxyl bond peak (M–OH; ~ 533.66 eV) attributed to the surface adsorbed water and/or the hydroxyl groups related to partially decomposed MOF-architecture (Figs. S11(a) and S11(c) in the ESM) [15]. Interestingly, the C 1s XPS spectra displayed mainly three peaks corresponding to *semi*-MOF related non-oxygenated C–C bonding peak (~ 284.78 eV), metal–oxygen unit (M–O–C at ~ 285.65 eV), and the carboxylate unit (O=C–O at ~ 289.09 eV) (Figs. S11(b) and S11(d) in the ESM) [5]. In particular, the O 1s and C 1s XPS spectral data emphasized the presence of partially decomposed MOF in both Ni-M@C-400 and Co-M@C-400.

3.2 Water electrolysis performance evaluation

3.2.1 *Oxygen evolution abilities*

At first, Ni-MOF and its CNT-composite have been tested for OER activity and noticed the significance of CNT in improving the performance. Subsequently, the annealed samples of Ni-MOF@CNT in the presence of Fe-vapor were scrutinized to elucidate the OER activities. Among the Fe-doped samples, the one prepared at relatively low annealing temperature (Ni-M@C-400) displayed enormously improved OER activity with very low overpotential of 229 mV to achieve the benchmark current density (10 mA/cm^2; η_{10}) (Fig. S12(a) in the ESM). The Ni-M@C-400 OER performance is extremely low compared to the commercial RuO_2 catalyst (266 mV at η_{10}), and the samples prepared at higher annealing temperatures (Ni-M@C-500: 299 mV at η_{10} and Ni-M@C-600: 326 mV at η_{10}). The improved OER performance of Ni-

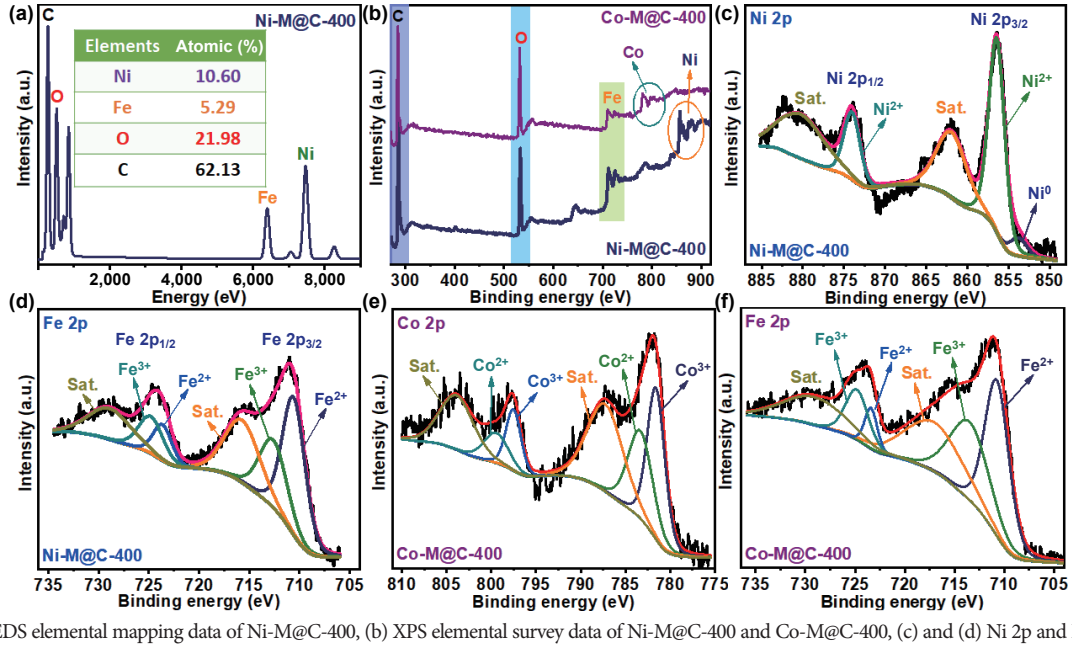

Figure 3 (a) EDS elemental mapping data of Ni-M@C-400, (b) XPS elemental survey data of Ni-M@C-400 and Co-M@C-400, (c) and (d) Ni 2p and Fe 2p core-level XPS data of Ni-M@C-400, and (e) and (f) Co 2p and Fe 2p core-level XPS data of Co-M@C-400.

M@C-400 clearly emphasized the importance of partially crumbled nanosheets with interconnected CNT fastened by active heteronanoparticles over the fully decomposed materials [32, 33, 38, 58]. While, the improved OER activity of Ni-M@C-400 and Ni-M@C-500 over the Ni-M@C-600 sample suggests the fact that the combination of heteronanoparticles ($Ni_{0.4}Fe_{2.6}O_4$ and Ni) is beneficial for OER performance over the sample with NiFe alloy particles alone in CNT-matrix (Fig. S12(a) in the ESM) [32]. Besides, the sample prepared without Fe-source (Ni@*semi*-MOF) displayed inferior OER performance (377 mV at η_{10}) compared to Ni-M@C-400, that signifies the importance of multi-metal combination for enhanced OER activity [13].

Moreover, the recent theoretical and experimental investigations approved that the heterometal-doping can modulate the electronic structure, electrical conductivity, number of active sites, and intrinsic characteristics of a material in order to reduce the free energy barrier of reaction intermediates and thereby significantly boost the OER activity [34, 41, 59]. Similarly, the annealed Ni-MOF without the integration of CNT (Ni-MOF-400) required a high overpotential of 383 mV (η_{10}), which is 154 mV high overpotential compared to the sample prepared with CNT (Ni-M@C-400) that highlights the significance of interconnected CNT-network [60]. Altogether, the overpotential detected for Ni-M@C-400 is one of the best OER performances detected so far on GCE including the pristine MOFs and MOF-derived composites (Table S1 in the ESM).

Interestingly, the OER performance of Ni-M@C-400 is much better than the conventional bimetallic MOF-derived NiFe-M@C-400 (270 mV at η_{10}) prepared under the same set of experimental conditions, which demonstrates the significance of vapor phased Fe-doing strategy over the traditional multi metal-doping (Fig. 4(a)). Similarly, Co-M@C-400 also displayed considerably improved OER activity (254 mV at η_{10}) over its bimetallic MOF-derivative (CoFe-M@C-400; 288 mV at η_{10}) in supporting the vaporized Fe-doping. This aforementioned comparative investigation suggests that the maximum decomposition taking place in bimetallic MOFs is not favorable for the OER application as most of the active sites possibly blocked by the bulk graphitic carbon produced during carbonization [32, 58]. While the controlled decomposition taking place in monometallic MOFs under Fe-vapor expected to yield active species in partially crumbled nanosheets and thereby displayed much better OER activity. Moreover, the high OER performances of Ni-M@C-400 and NiFe-M@C-400 over the Co/Fe-based catalysts suggest the significance of heteronanoparticles combination ($Ni_{0.4}Fe_{2.6}O_4$/Ni) over the existence of $CoFe_2O_4$ nanoparticles alone in CNT. Besides, among the other *semi*-MOFs, Cu-M@C-400 (297 mV at η_{10}) exhibited considerably better OER activity over the other electrocatalysts, Cr-M@C-400 (342 mV at η_{10}) and Mn-M@C-400 (327 mV at η_{10}), possibly owing to the heteronanoparticles synergism.

In addition to the superior OER activity, Ni-M@C-400 also displayed very low Tafel slope (40.51 mV/dec) by keeping its superiority in overwhelming the thermodynamic barrier. Although the other Fe-doped samples fabricated at higher annealing temperature require large overpotentials, they do exhibit feasible OER kinetics (Ni-M@C-500: 43.97 mV/dec and Ni-M@C-600: 47.05 mV/dec) signifying the superiority of Ni/Fe-based OER catalysts, over the benchmark RuO_2 catalyst (52.56 mV/dec). Although, the Tafel slopes of CoFe-based *semi*-MOFs are slightly higher than the Ni/Fe-based *semi*-MOFs, they are significantly better than state-of-the-art RuO_2 electrocatalyst (Fig. 4(b)). To our surprise, the other *semi*-MOFs including Cr-M@C-400, Mn-M@C-400, and Cu-M@C-400 displayed surprisingly higher Tafel slopes despite showing appreciable OER activity (Fig. S13 in the ESM), which demonstrates the feasibility of Ni/Fe- and Co/Fe-combinations in lowering the thermodynamic barrier for OER [60, 61].

Moreover, the estimated electrochemical surface area from cyclic voltammograms operated within non-Faradic capacitive current range approved the enlarged C_{dl} values for Ni-M@C-400 (5.63 mF/cm^2) and Co-M@C-400 (3.17 mF/cm^2) over the corresponding bimetallic counterparts (NiFe-M@C-400: 2.36 mF/cm^2 and CoFe-M@C-400: 1.73 mF/cm^2), which suggests the availability of high electrochemically accessible surface area and also confirms the highest possibility of active sites exposure at the electrode/electrolyte interface for the improved OER activity (Fig. 4(c) and Fig. S14 in the ESM). In addition, a very low charge transfer resistance (R_{ct}) was observed for the *semi*-MOF derivatives, including Ni-M@C-400 (8.23 Ω), NiFe-M@C-400

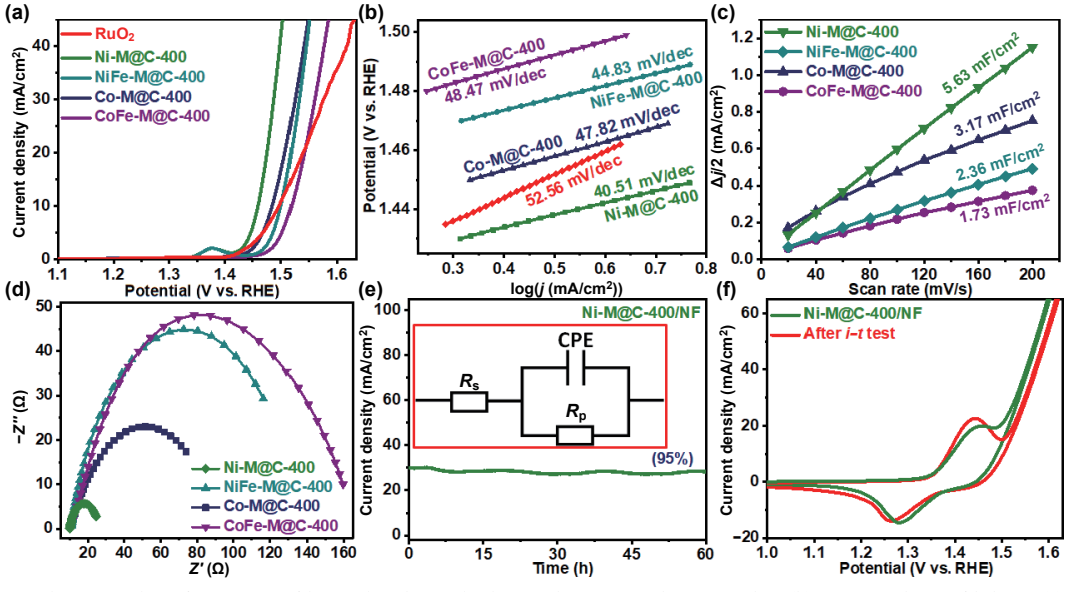

Figure 4 (a) LSV polarization plots of *semi*-MOFs fabricated in this study along with commercial RuO_2 catalyst, (b) corresponding Tafel slopes, (c) electrochemical active surface area elucidated from cyclic voltammograms, (d) Nyquist plots of *semi*-MOFs at an overpotential of 229 mV, (e) chronoamperometric (*i*–*t*) test on Ni-M@C-400/NF at a current density of 30 mA/cm^2 (inset shows the equivalent circuit diagram of EIS data), and (f) CV curves of Ni-M@C-400/NF before and after *i*–*t* test.

(10.63 Ω), Co-M@C-400 (10.30 Ω), and CoFe-M@C-400 (11.77 Ω) in electrochemical impedance spectroscopy measured at a fixed 229 mV overpotential (Fig. 4(d)), among which Ni-M@C-400 displayed the smallest value of R_{ct}. Overall, Ni-M@C-400 established to be one of the best OER electrocatalysts reported to date owing to its partial MOF-features, heteronanoparticles synergism, mechanical stability, and electrical conductivity enhancement of CNT-network and largely exposed active catalytic sites with smallest charge transfer resistance. Besides, Ni-M@C-400/NF also displayed exceptional durability in a 60 h *i–t* test conducted at a current density of 30 mA/cm^2 and the CV plots obtained before and after the *i–t* test are almost identical (Figs. 4(e) and 4(f)).

3.2.2 *Post-OER investigations*

In general, transition metal-based electrocatalysts undergo *in situ* surface oxidation during OER process and the modified surface is considered as the actual catalytic site for OER activity [62, 63]. As can be seen in Fig. 4(a), the small redox peak appeared (~ 1.38 V) prior to the OER onset potential for both Ni-M@C-400 and NiFe-M@C-400 signify that the surface of those materials is getting converted to oxidized phase and is served as the actual catalytic site for OER process [64]. Moreover, in most Ni/Fe-based electrocatalysts, Ni is considered as the active species for OER application and the Fe-source expected to adjust the surface electronic states of Ni (Ni^{2+} to $Ni^{3+/4+}$) during redox process in order to enhance the OER activity [25, 65]. And in most cases, the OER proceeds via Ni–O(OH) and/or Fe–O(OH) layer formation [54, 66], while the complete transformation of a material during water oxidation is scarcely noticed [15, 49, 67]. Therefore, in order to elucidate the real catalytic sites in Ni-M@C-400, the sample after 2,000 CV cycles has been analyzed. Despite delivering almost the same LSV plot after 2,000 CV cycles (Fig. 5(a)), the material transformed its morphology into porous mesh-like CNT-framework with randomly exposed bright Ni nanoparticles (Fig. S15 in the ESM). In addition, no clear evidence of any other crystalline phases was detected in its XRD analysis after OER cycling and approved the *semi*-MOF composition with $Ni_{0.4}Fe_{2.6}O_4$ and Ni heteronanoparticles, suggesting the robust structural stability (Fig. 5(b)).

Moreover, captivating binding energy dislocation has been detected in Fe 2p XPS spectra of Ni-M@C-400 after OER, wherein the peaks correspond to Fe^{2+} and Fe^{3+} shifted to (~ 1.18 to 2.28 eV) higher binding energy, confirming the elevated 3d-electron density in Fe towards forming the oxyhydroxide (Fe–O(OH)) intermediate in order to facilitate the OER catalysis (Fig. 5(c)) [65, 68]. Additionally, the metal–oxygen peak in O 1s spectra slightly moved to lower binding energy (0.25 eV) in approving the new metal–O(OH) formation (Fig. S16(b) in the ESM) [65], which means a slight portion of Fe-doped surface ($Ni_{0.4}Fe_{2.6}O_4$) transformed to Fe–O(OH) layer during water oxidation and the internal composition is same as before, this hypothesis was also supported by the new broad peak correspond to Fe–O(OH) phase appeared at 505–620 cm^{-1} in its Raman analysis (Fig. 5(d)) [40, 69]. In general, the Raman peaks correspond to $Ni_{0.4}Fe_{2.6}O_4$ (322 cm^{-1} (T^3_{2g}), 567 cm^{-1} (T^2_{2g}), and 674 cm^{-1} (A_{1g})) appeared in this region and the intensified peak appearance after OER suggests that the surface occupied nickel ferrite material is basically transformed to Fe–O(OH) layer during OER cycles and the internal composition is unaffected [70, 71]. Therefore, based on the post-OER characterizations, we believe that the surface occupied $Ni_{0.4}Fe_{2.6}O_4$ material mainly transformed to Fe–O(OH) layer during OER catalysis and the synergistic interactions between Fe–O(OH) layer and the unaffected internal composition are the actual reaction sites for OER application.

Considering the remarkable OER activity of Ni-M@C-400, overall water splitting ability of this *semi*-MOF electrocatalyst has been evaluated by constructing a two-electrode system with commercial Pt/C (as cathode) [5, 40, 72]. As can be seen in Fig. S17(c) in the ESM, significantly better full water splitting performance was noticed for Pt/C@NF||Ni-M@C-400@NF combination over commercial Pt/C@NF||RuO_2@NF combination on nickel foam current collectors (loading of 2 mg/cm^2) particularly at higher current densities. In particular, a low cell voltage of 1.76 V is required for Pt/C@NF||Ni-M@C-400@NF combination to achieve the current density of 50 mA/cm^2, while a high potential of 142 mV is needed for the commercial electrocatalysts combination to achieve the same current density (1.902 V at η_{50}). Additionally, Ni-M@C-400 loaded Ni foam

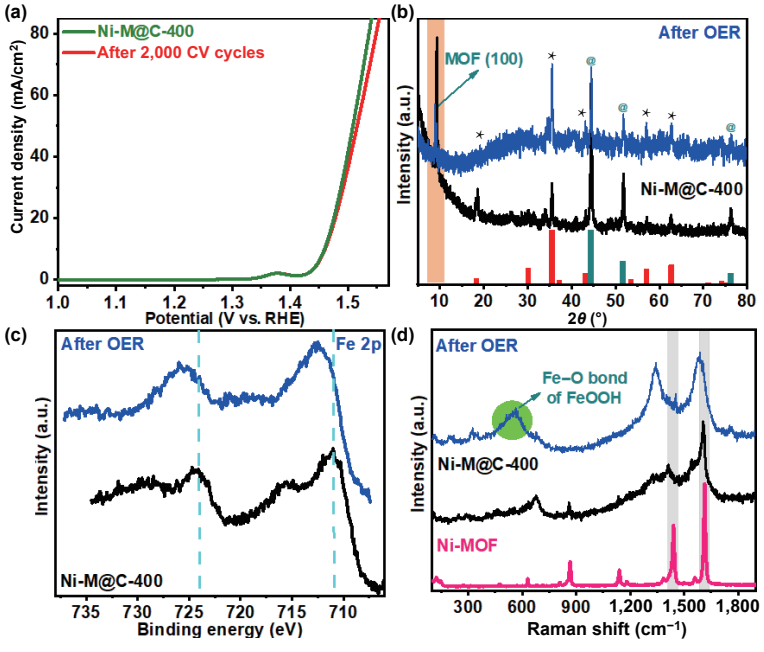

Figure 5 (a) LSV curves of Ni-M@C-400 before and after 2,000 continuous CV cycles, (b) XRD data of Ni-M@C-400 before and after OER CV cycles, (c) core-level Fe 2p XPS spectra of Ni-M@C-400 before and after OER cycles, and (d) the comparison of Raman spectra of Ni-MOF and Ni-M@C-400 before and after OER CV cycling test.

substrates combination (Ni-M@C-400@NF alone) also displayed noteworthy full water splitting performance (1.95 V at η_{50}) but is significantly lower than the Pt/C@NF||Ni-M@C-400@NF combination owing to the inadequate HER activity of Ni-M@C-400 (209 mV at η_{10}, Fig. S17(b) in the ESM). Besides that, Faraday efficiency (FE) of this Pt/C@NF||Ni-M@C-400@NF combination has been elucidated by collecting the H_2 and O_2 gases released during overall water splitting catalysis. Specifically, ~ 15 mL of H_2 and ~ 7.5 mL of O_2 gases have been collected by a lab-made water drainage system (Fig. S18 in the ESM) [ESM) [73, 74] and the v/v of obtained H_2:O_2 represents the theoretical ratio of 2:1, confirming that the employed electric current is exclusively used for the water spitting catalysis and hence the estimated FE for both HER and OER is about 100% (Fig. S17(d) in the ESM).

4 Conclusions

This study establishes the novel surface engineering strategy to transform the material surface into secondary-metal doped composition. As the secondary metal-doped at a regulated carbonization conditions, the obtained materials surface is different from its internal composition leading to the hetero-composition synergism. Owing to the combined structural features related to MOF-architecture, electrochemically active heteronanoparticles synergism, interconnected conductive CNT-network electrical and mechanical support, as-obtained *semi*-MOF systems displayed noteworthy OER activity. The post-OER characterizations revealed the fact that the surface occupied $Ni_{0.4}Fe_{2.6}O_4$ transformed to Fe–O(OH) layer during OER catalysis and its productive synergism with unaffected internal composition is the actual reason for improved OER. This work also demonstrates the versatility of sublimated Fe-doping strategy and among the variety of composites, Ni- and Co- *semi*-MOFs displayed their dominance over commercial RuO_2 in terms of OER performance and lowering the thermodynamic barrier. The proposed generalized Fe-doping strategy can open up the path towards disclosing the universally acceptable approaches in order to design and fabricate the advanced electrocatalysts for water electrolysis.

Acknowledgements

The research was financially supported by the National Natural Science Foundation of China (Nos. 21773024 and 52072310), Sichuan Science and Technology Program (No. 20YYJC3786), China Postdoctoral Science Foundation (No. 2019M663469), and the Reformation and Development Funds for Local Region Universities from China Government in 2020 (No. ZCKJ 2020-11).

Electronic Supplementary Material: Supplementary material (schematic of Ni-MOF@CNT annealed at different temperatures, XRD patterns, Raman data, SEM images of control samples, additional TEM images and XPS data, additional LSV curves and cyclic voltammograms, HER LSV plots, overall water splitting curves, Faraday efficiency calculation, plots, and corresponding photographs) is available in the online version of this article at https://doi.org/10.1007/s12274-022-4231-8.

References

[1] Chu, S; Majumdar, A. Opportunities and challenges for a sustainable energy future. *Nature* **2012**, *488*, 294–303.

[2] Zhou, T. P.; Shan, H.; Yu, H.; Zhong, C. A.; Ge, J. K.; Zhang, N.; Chu, W. S.; Yan, W. S.; Xu, Q.; Wu, H. A. et al. Nanopore confinement of electrocatalysts optimizing triple transport for an ultrahigh-power-density zinc-air fuel cell with robust stability. *Adv. Mater.* **2020**, *32*, 2003251.

[3] Gao, C. B.; Lyu, F. L.; Yin, Y. D. Encapsulated metal nanoparticles for catalysis. *Chem. Rev.* **2021**, *121*, 834–881.

[4] Qin, T. C.; Wang, Z. G.; Wang, Y. Q.; Besenbacher, F.; Otyepka, M.; Dong, M. D. Recent progress in emerging two-dimensional transition metal carbides. *Nano-Micro Lett.* **2021**, *13*, 183.

[5] Srinivas, K.; Chen, Y. F.; Wang, B.; Yu, B.; Wang, X. Q.; Hu, Y.; Lu, Y. J.; Li, W. X.; Zhang, W. L.; Yang, D. X. Metal-organic framework-derived NiS/Fe_3O_4 heterostructure-decorated carbon nanotubes as highly efficient and durable electrocatalysts for oxygen evolution reaction. *ACS Appl. Mater. Interfaces* **2020**, *12*, 31552–31563.

[6] Wang, Y. M.; Qian, G. F.; Xu, Q. L.; Zhang, H.; Shen, F.; Luo, L.; Yin, S. B. Industrially promising $IrNi-FeNi_3$ hybrid nanosheets for overall water splitting catalysis at large current density. *Appl. Catal. B:Environ.* **2021**, *286*, 119881.

[7] Che, Z. W.; Lu, X. Y.; Cai, B. F.; Xu, X. X.; Bao, J. C.; Liu, Y. Ligand-controlled synthesis of high density and ultra-small Ru nanoparticles with excellent electrocatalytic hydrogen evolution performance. *Nano Res.* **2022**, *15*, 1269–1275.

[8] Li, X. Y.; Xiao, L. P.; Zhou, L.; Xu, Q. C.; Weng, J.; Xu, J.; Liu, B. Adaptive bifunctional electrocatalyst of amorphous CoFe oxide@2D black phosphorus for overall water splitting. *Angew. Chem., Int. Ed.* **2020**, *59*, 21106–21113.

[9] Wang, Q.; Astruc, D. State of the art and prospects in metal-organic framework (MOF)-based and MOF-derived nanocatalysis. *Chem. Rev.* **2020**, *120*, 1438–1511.

[10] Wang, W. B.; Yang, Y.; Zhao, Y.; Wang, S. Z.; Ai, X. M.; Fang, J. K.; Liu, Y. W. Multi-scale regulation in S, N co-incorporated carbon encapsulated Fe-doped Co_9S_8 achieving efficient water oxidation with low overpotential. *Nano Res.* **2022**, *15*, 872–880.

[11] Zhong, D. Z.; Li, T.; Wang, D.; Li, L. N.; Wang, J. C.; Hao, G. Y.; Liu, G.; Zhao, Q.; Li, J. P. Strengthen metal–oxygen covalency of CoFe-layered double hydroxide for efficient mild oxygen evolution. *Nano Res.* **2022**, *15*, 162–169.

[12] Yang, D. X.; Chen, Y. F.; Su, Z.; Zhang, X. J.; Zhang, W. L.; Srinivas, K. Organic carboxylate-based MOFs and derivatives for electrocatalytic water oxidation. *Coord. Chem. Rev.* **2021**, *428*, 213619.

[13] Li, F. L.; Shao, Q.; Huang, X. Q.; Lang, J. P. Nanoscale trimetallic metal-organic frameworks enable efficient oxygen evolution electrocatalysis. *Angew. Chem., Int. Ed.* **2018**, *57*, 1888–1892.

[14] Sun, F. Z.; Wang, G.; Ding, Y. Q.; Wang, C.; Yuan, B. B.; Lin, Y. Q. NiFe-based metal-organic framework nanosheets directly supported on nickel foam acting as robust electrodes for electrochemical oxygen evolution reaction. *Adv. Energy Mater.* **2018**, *8*, 1800584.

[15] Luo, X.; Ji, P. X.; Wang, P. Y.; Cheng, R. L.; Chen, D.; Lin, C.; Zhang, J. N.; He, J. W.; Shi, Z. H.; Li, N. et al. Interface engineering of hierarchical branched Mo-doped Ni_3S_2/Ni_xP_y hollow heterostructure nanorods for efficient overall water splitting. *Adv. Energy Mater.* **2020**, *10*, 1903891.

[16] Gu, X. K.; Camayang, J. C. A.; Samira, S.; Nikolla, E. Oxygen evolution electrocatalysis using mixed metal oxides under acidic conditions: Challenges and opportunities. *J. Catal.* **2020**, *388*, 130–140.

[17] Wang, X. Y.; He, Y.; Han, X. P.; Zhao, J.; Li, L. L.; Zhang, J. F.; Zhong, C.; Deng, Y. D.; Hu, W. B. Engineering cobalt sulfide/oxide heterostructure with atomically mixed interfaces for synergistic electrocatalytic water splitting. *Nano Res.* **2022**, *15*, 1246–1253.

[18] Wang, Z. G.; Wu, H. H.; Li, Q.; Besenbacher, F.; Li, Y. R.; Zeng, X. C.; Dong, M. D. Reversing interfacial catalysis of ambipolar WSe_2 single crystal. *Adv. Sci.* **2020**, *7*, 1901382.

[19] Deng, Y. J.; Chi, B.; Li, J.; Wang, G. H.; Zheng, L.; Shi, X. D.; Cui, Z. M.; Du, L.; Liao, S. J.; Zang, K. T. et al. Atomic Fe-doped MOF-derived carbon polyhedrons with high active-center density and ultra-high performance toward PEM fuel cells. *Adv. Energy Mater.* **2019**, *9*, 1802856.

[20] Chen, J. Y.; Zhuang, P. Y.; Ge, Y. C.; Chu, H.; Yao, L. Y.; Cao, Y. D.; Wang, Z. Y.; Chee, M. O. L.; Dong, P.; Shen, J. F. et al. Sublimation-vapor phase pseudomorphic transformation of template-

directed MOFs for efficient oxygen evolution reaction. *Adv. Funct. Mater.* **2019**, *29*, 1903875.

[21] Gao, R.; Yan, D. P. Recent development of Ni/Fe-based micro/nanostructures toward photo/electrochemical water oxidation. *Adv. Energy Mater.* **2020**, *10*, 1900954.

[22] Zhao, X. J.; Pachfule, P.; Li, S.; Simke, J. R. J.; Schmidt, J.; Thomas, A. Bifunctional electrocatalysts for overall water splitting from an iron/nickel-based bimetallic metal-organic framework/dicyandiamide composite. *Angew. Chem.* **2018**, *130*, 9059–9064.

[23] Wang, M.; Wang, Y. Q.; Mao, S. S.; Shen, S. H. Transition-metal alloy electrocatalysts with active sites modulated by metal-carbide heterophases for efficient oxygen evolution. *Nano Energy* **2021**, *88*, 106216.

[24] Zhang, W.; Li, D. H.; Zhang, L. Z.; She, X. L.; Yang, D. J. NiFe-based nanostructures on nickel foam as highly efficiently electrocatalysts for oxygen and hydrogen evolution reactions. *J. Energy Chem.* **2019**, *39*, 39–53.

[25] Anantharaj, S.; Kundu, S.; Noda, S. "The Fe effect" : A review unveiling the critical roles of Fe in enhancing OER activity of Ni and Co based catalysts. *Nano Energy* **2021**, *80*, 105514.

[26] Chang, J. L.; Chen, L. M.; Zang, S. Q.; Wang, Y. F.; Wu, D. P.; Xu, F.; Jiang, K.; Gao, Z. Y. The effect of Fe(III) cations in electrolyte on oxygen evolution catalytic activity of $Ni(OH)_2$ electrode. *J. Colloid Interface Sci.* **2020**, *569*, 50–56.

[27] Ren, J. T.; Yuan, G. G.; Weng, C. C.; Chen, L.; Yuan, Z. Y. Uniquely integrated Fe-doped $Ni(OH)_2$ nanosheets for highly efficient oxygen and hydrogen evolution reactions. *Nanoscale* **2018**, *10*, 10620–10628.

[28] Zhong, B.; Kuang, P. Y.; Wang, L. X.; Yu, J. G. Hierarchical porous nickel supported $NiFeO_xH_y$ nanosheets for efficient and robust oxygen evolution electrocatalyst under industrial condition. *Appl. Catal. B:Environ.* **2021**, *299*, 120668.

[29] Tian, G. Q.; Wei, S. R.; Guo, Z. T.; Wu, S. W.; Chen, Z. L.; Xu, F. M.; Cao, Y.; Liu, Z.; Wang, J. Q.; Ding, L. et al. Hierarchical $NiMoP_2$-Ni_2P with amorphous interface as superior bifunctional electrocatalysts for overall water splitting. *J. Mater. Sci. Technol.* **2021**, *77*, 108–116.

[30] Wang, X. Q.; Wang, B.; Chen, Y. F.; Wang, M. Y.; Wu, Q.; Srinivas, K.; Yu, B.; Zhang, X. J.; Ma, F.; Zhang, W. L. Fe_2P nanoparticles embedded on Ni_2P nanosheets as highly efficient and stable bifunctional electrocatalysts for water splitting. *J. Mater. Sci. Technol.* **2022**, *105*, 266–273.

[31] Yang, D. X.; Su, Z.; Chen, Y. F.; Srinivas, K.; Gao, J. Z.; Zhang, W. L.; Wang, Z. G.; Lin, H. P. Electronic modulation of hierarchical spongy nanosheets toward efficient and stable water electrolysis. *Small* **2021**, *17*, 2006881.

[32] Wang, X. L.; Xiao, H.; Li, A.; Li, Z.; Liu, S. J.; Zhang, Q. H.; Gong, Y.; Zheng, L. R.; Zhu, Y. Q.; Chen, C. et al. Constructing $NiCo/Fe_3O_4$ heteroparticles within MOF-74 for efficient oxygen evolution reactions. *J. Am. Chem. Soc.* **2018**, *140*, 15336–15341.

[33] Zhao, M.; Li, W.; Li, J. Y.; Hu, W. H.; Li, C. M. Strong electronic interaction enhanced electrocatalysis of metal sulfide clusters embedded metal-organic framework ultrathin nanosheets toward highly efficient overall water splitting. *Adv. Sci.* **2020**, *7*, 2001965.

[34] Dou, S.; Dong, C. L.; Hu, Z.; Huang, Y. C.; Chen, J. L.; Tao, L.; Yan, D. F.; Chen, D. W.; Shen, S. H.; Chou, S. L. et al. Atomic-scale CoO_x species in metal-organic frameworks for oxygen evolution reaction. *Adv. Funct. Mater.* **2017**, *27*, 1702546.

[35] Liu, T.; Li, P.; Yao, N.; Cheng, G. Z.; Chen, S. L.; Luo, W.; Yin, Y. D. CoP-doped MOF-based electrocatalyst for pH-universal hydrogen evolution reaction. *Angew. Chem., Int. Ed.* **2019**, *58*, 4679–4684.

[36] Wu, X. Q.; Huang, D. D.; Wu, Y. P.; Zhao, J.; Liu, X.; Dong, W. W.; Li, S.; Li, D. S.; Li, J. R. *In situ* synthesis of nano CuS-embedded MOF hierarchical structures and application in dye adsorption and hydrogen evolution reaction. *ACS Appl. Energy Mater.* **2019**, *2*, 5698–5706.

[37] Srinivas, K.; Chen, Y. F.; Wang, B.; Yu, B.; Lu, Y. J.; Su, Z.; Zhang, W. L.; Yang, D. X. Metal-organic framework-derived Fe-doped $Ni_3Fe/NiFe_2O_4$ heteronanoparticle-decorated carbon nanotube network as a highly efficient and durable bifunctional electrocatalyst. *ACS Appl. Mater. Interfaces* **2020**, *12*, 55782–55794.

[38] Srinivas, K.; Chen, Y. F.; Wang, X. Q.; Wang, B.; Karpuraranjith, M.; Wang, W.; Su, Z.; Zhang, W. L.; Yang, D. X. Constructing Ni/NiS heteronanoparticle-embedded metal-organic framework-derived nanosheets for enhanced water-splitting catalysis. *ACS Sustainable Chem. Eng.* **2021**, *9*, 1920–1931.

[39] Yang, D. X.; Su, Z.; Chen, Y. F.; Srinivas, K.; Zhang, X. J.; Zhang, W. L.; Lin, H. P. Self-reconstruction of a MOF-derived chromium-doped nickel disulfide in electrocatalytic water oxidation. *Chem. Eng. J.* **2022**, *430*, 133046.

[40] Yang, D. X.; Su, Z.; Chen, Y. F.; Lu, Y. J.; Yu, B.; Srinivas, K.; Wang, B.; Zhang, W. L. Double-shelled hollow bimetallic phosphide nanospheres anchored on nitrogen-doped graphene for boosting water electrolysis. *J. Mater. Chem. A* **2020**, *8*, 22222–22229.

[41] Zhu, K. Y.; Chen, J. Y.; Wang, W. J.; Liao, J. W.; Dong, J. C.; Chee, M. O. L.; Wang, N.; Dong, P.; Ajayan, P. M.; Gao, S. P. et al. Etching-doping sedimentation equilibrium strategy: Accelerating kinetics on hollow Rh-doped CoFe-layered double hydroxides for water splitting. *Adv. Funct. Mater.* **2020**, *30*, 2003556.

[42] Chen, J. W.; Wang, F. M.; Qi, X. P.; Yang, H.; Peng, B. J.; Xu, L.; Xiao, Z. L.; Hou, X. M.; Liang, T. X. A simple strategy to construct cobalt oxide-based high-efficiency electrocatalysts with oxygen vacancies and heterojunctions. *Electrochim. Acta* **2019**, *326*, 134979.

[43] Ren, C. T.; Jia, X.; Zhang, W.; Hou, D.; Xia, Z. Q.; Huang, D. S.; Hu, J.; Chen, S. P.; Gao, S. L. Hierarchical porous integrated $Co_{1-x}S/CoFe_2O_4$@rGO nanoflowers fabricated via temperature-controlled *in situ* calcining sulfurization of multivariate CoFe-MOF-74@rGO for high-performance supercapacitor. *Adv. Funct. Mater.* **2020**, *30*, 2004519.

[44] Yang, L. J.; Li, H.; Yu, Y.; Wu, Y.; Zhang, L. Assembled 3D MOF on 2D nanosheets for self-boosting catalytic synthesis of N-doped carbon nanotube encapsulated metallic Co electrocatalysts for overall water splitting. *Appl. Catal. B:Environ.* **2020**, *271*, 118939.

[45] Abdel-Wahed, M. S.; El-Kalliny, A. S.; Badawy, M. I.; Attia, M. S.; Gad-Allah, T. A. Core double-shell $MnFe_2O_4$@rGO@TiO_2 superparamagnetic photocatalyst for wastewater treatment under solar light. *Chem. Eng. J.* **2020**, *382*, 122936.

[46] Wang, B.; Wang, X. Q.; Wang, Z. G.; Srinivas, K.; Zhang, X. J.; Yu, B.; Yang, D. X.; Zhang, W. L.; Lau, T. C.; Chen, Y. F. Electronic modulation of NiS-PBA/CNT with boosted water oxidation performance realized by a rapid microwave-assisted *in-situ* partial sulfidation. *Chem. Eng. J.* **2021**, *420*, 130481.

[47] Ma, F.; Yu, B.; Zhang, X. J.; Zhang, Z. H.; Srinivas, K.; Wang, X. Q.; Liu, D. W.; Wang, B.; Zhang, W. L.; Wu, Q. et al. $WN_{0.67}$-embedded N-doped graphene-nanosheet interlayer as efficient polysulfide catalyst and absorbant for high-performance lithium-sulfur batteries. *Chem. Eng. J.* **2022**, *431*, 133439.

[48] Lu, Y. J.; Chen, Y. F.; Srinivas, K.; Su, Z.; Wang, X. Q.; Wang, B.; Yang, D. X. Employing dual-ligand co-coordination compound to construct nanorod-like Bi-metallic (Fe, Co)P decorated with nitrogen-doped graphene for electrocatalytic overall water splitting. *Electrochim. Acta* **2020**, *350*, 136338.

[49] Rui, K.; Zhao, G. Q.; Chen, Y. P.; Lin, Y.; Zhou, Q.; Chen, J. Y.; Zhu, J. X.; Sun, W. P.; Huang, W.; Dou, S. X. Hybrid 2D dual-metal-organic frameworks for enhanced water oxidation catalysis. *Adv. Funct. Mater.* **2018**, *28*, 1801554.

[50] Kamble, R. B.; Varade, V.; Ramesh, K. P.; Prasad, V. Domain size correlated magnetic properties and electrical impedance of size dependent nickel ferrite nanoparticles. *AIP Adv.* **2015**, *5*, 017119.

[51] Sankar, K. V.; Selvan, R. K.; Meyrick, D. Electrochemical performances of $CoFe_2O_4$ nanoparticles and a rGO based asymmetric supercapacitor. *RSC Adv.* **2015**, *5*, 99959–99967.

[52] Zhu, P.; Gao, J. X.; Liu, S. Facile *in situ* coupling CoFe/Co nanoparticles and N-doped carbon nanotubes/graphitic nanosheets as bifunctional oxygen electrocatalysts for rechargeable Zn-air batteries. *J. Power Sources* **2020**, *449*, 227512.

[53] Liu, J. L.; Zhu, D. D.; Ling, T.; Vasileff, A.; Qiao, S. Z. S-$NiFe_2O_4$ ultra-small nanoparticle built nanosheets for efficient water splitting in alkaline and neutral pH. *Nano Energy* **2017**, *40*, 264–273.

[54] Li, F. L.; Wang, P. T.; Huang, X. Q.; Young, D. J.; Wang, H. F.; Braunstein, P.; Lang, J. P. Large-scale, bottom-up synthesis of binary metal-organic framework nanosheets for efficient water

oxidation. *Angew. Chem., Int. Ed.* **2019**, *58*, 7051–7056.
[55] Zhang, J. F.; Jiang, Y.; Wang, Y.; Yu, C. P.; Cui, J. W.; Wu, J. J.; Shu, X.; Qin, Y. Q.; Sun, J.; Yan, J. et al. Ultrathin carbon coated mesoporous Ni-$NiFe_2O_4$ nanosheet arrays for efficient overall water splitting. *Electrochim. Acta* **2019**, *321*, 134652.
[56] Li, S. S.; Sirisomboonchai, S.; Yoshida, A.; An, X. W.; Hao, X. G.; Abudula, A.; Guan, G. Q. Bifunctional CoNi/$CoFe_2O_4$/Ni foam electrodes for efficient overall water splitting at a high current density. *J. Mater. Chem. A* **2018**, *6*, 19221–19230.
[57] Lei, S.; Li, Q. H.; Kang, Y.; Gu, Z. G.; Zhang, J. Epitaxial growth of oriented prussian blue analogue derived well-aligned $CoFe_2O_4$ thin film for efficient oxygen evolution reaction. *Appl. Catal. B:Environ.* **2019**, *245*, 1–9.
[58] Srinivas, K.; Lu, Y. J.; Chen, Y. F.; Zhang, W. L.; Yang, D. X. $FeNi_3$-Fe_3O_4 heterogeneous nanoparticles anchored on 2D MOF nanosheets/1D CNT matrix as highly efficient bifunctional electrocatalysts for water splitting. *ACS Sustainable Chem. Eng.* **2020**, *8*, 3820–3831.
[59] Mohanty, B.; Bhanja, P.; Jena, B. K. An overview on advances in design and development of materials for electrochemical generation of hydrogen and oxygen. *Mater. Today Energy* **2022**, *23*, 100902.
[60] Muschi, M.; Serre, C. Progress and challenges of graphene oxide/metal–organic composites. *Coord. Chem. Rev.* **2019**, *387*, 262–272.
[61] Shao, Q.; Wang, P. T.; Huang, X. Q. Opportunities and challenges of interface engineering in bimetallic nanostructure for enhanced electrocatalysis. *Adv. Funct. Mater.* **2019**, *29*, 1806419.
[62] Huang, J. W.; Li, Y. Y.; Zhang, Y. D.; Rao, G. F.; Wu, C. Y.; Hu, Y.; Wang, X. F.; Lu, R. F.; Li, Y. R.; Xiong, J. Identification of key reversible intermediates in self-reconstructed nickel-based hybrid electrocatalysts for oxygen evolution. *Angew. Chem., Int. Ed.* **2019**, *58*, 17458–17464.
[63] Görlin, M.; de Araújo, J. F.; Schmies, H.; Bernsmeier, D.; Dresp, S.; Gliech, M.; Jusys, Z.; Chernev, P.; Kraehnert, R.; Dau, H. et al. Tracking catalyst redox states and reaction dynamics in Ni-Fe oxyhydroxide oxygen evolution reaction electrocatalysts: The role of catalyst support and electrolyte pH. *J. Am. Chem. Soc.* **2017**, *139*, 2070–2082.
[64] Dionigi, F.; Zeng, Z. H.; Sinev, I.; Merzdorf, T.; Deshpande, S.; Lopez, M. B.; Kunze, S.; Zegkinoglou, I.; Sarodnik, H.; Fan, D. X. et al. *In-situ* structure and catalytic mechanism of NiFe and CoFe layered double hydroxides during oxygen evolution. *Nat. Commun.* **2020**, *11*, 2522.
[65] Qian, Q. Z.; Li, Y. P.; Liu, Y.; Yu, L.; Zhang, G. Q. Ambient fast synthesis and active sites deciphering of hierarchical foam-like trimetal-organic framework nanostructures as a platform for highly efficient oxygen evolution electrocatalysis. *Adv. Mater.* **2019**, *31*, 1901139.
[66] Li, J. W.; Song, J. D.; Huang, B. Y.; Liang, G. F.; Liang, W. L.; Huang, G. J.; Jin, Y. Q.; Zhang, H.; Xie, F. Y.; Chen, J. et al. Enhancing the oxygen evolution reaction performance of NiFeOOH electrocatalyst for Zn-air battery by N-doping. *J. Catal.* **2020**, *389*, 375–381.
[67] Wang, P. Y.; Pu, Z. H.; Li, W. Q.; Zhu, J. W.; Zhang, C. T.; Zhao, Y. F.; Mu, S. C. Coupling $NiSe_2$–Ni_2P heterostructure nanowrinkles for highly efficient overall water splitting. *J. Catal.* **2019**, *377*, 600–608.
[68] Fang, M.; Han, D.; Xu, W. B.; Shen, Y.; Lu, Y. M.; Cao, P. J.; Han, S.; Xu, W. Y.; Zhu, D. L.; Liu, W. J. et al. Surface-guided formation of amorphous mixed-metal oxyhydroxides on ultrathin MnO_2 nanosheet arrays for efficient electrocatalytic oxygen evolution. *Adv. Energy Mater.* **2020**, *10*, 2001059.
[69] Chen, H. J.; Zou, Y. H.; Li, J.; Zhang, K. W.; Xia, Y. Z.; Hui, B.; Yang, D. J. Wood aerogel-derived sandwich-like layered nanoelectrodes for alkaline overall seawater electrosplitting. *Appl. Catal. B:Environ.* **2021**, *293*, 120215.
[70] Karpuraranjith, M.; Chen, Y. F.; Wang, B.; Ramkumar, J.; Yang, D. X.; Srinivas, K.; Wang, W.; Zhang, W. L.; Manigandan, R. Hierarchical ultrathin layered MoS_2@$NiFe_2O_4$ nanohybrids as a bifunctional catalyst for highly efficient oxygen evolution and organic pollutant degradation. *J. Colloid Interface Sci.* **2021**, *592*, 385–396.
[71] Wang, B.; Srinivas, K.; Wang, X. Q.; Su, Z.; Yu, B.; Zhang, X. J.; Liu, Y. F.; Ma, F.; Yang, D. X.; Chen, Y. F. Self-assembled $CoSe_2$–$FeSe_2$ heteronanoparticles along the carbon nanotube network for boosted oxygen evolution reaction. *Nanoscale* **2021**, *13*, 9651–9658.
[72] Srinivas, K.; Chen, Y. F.; Su, Z.; Yu, B.; Karpuraranjith, M.; Ma, F.; Wang, X. Q.; Zhang, W. L.; Yang, D. X. Heterostructural $CoFe_2O_4$/CoO nanoparticles-embedded carbon nanotubes network for boosted overall water-splitting performance. *Electrochim. Acta* **2022**, *404*, 139745.
[73] Hoa, V. H.; Tran, D. T.; Nguyen, D. C.; Kim, D. H.; Kim, N. H.; Lee, J. H. Molybdenum and phosphorous dual doping in cobalt monolayer interfacial assembled cobalt nanowires for efficient overall water splitting. *Adv. Funct. Mater.* **2020**, *30*, 2002533.
[74] Li, W.; Gao, X. F.; Xiong, D. H.; Xia, F.; Liu, J.; Song, W. G.; Xu, J. Y.; Thalluri, S. M.; Cerqueira, M. F.; Fu, X. L. et al. Vapor-solid synthesis of monolithic single-crystalline CoP nanowire electrodes for efficient and robust water electrolysis. *Chem. Sci.* **2017**, *8*, 2952–2958.